Interlayer ferromagnetism and high-temperature quantum anomalous Hall effect in *p*-doped MnBi$_2$Te$_4$ multilayers

Yulei Han [ORCID],[1] Shiyang Sun,[2] Shifei Qi,[2,1,*] Xiaohong Xu,[3,†] and Zhenhua Qiao [ORCID][1,‡]

[1]*ICQD, Hefei National Laboratory for Physical Sciences at Microscale, CAS Key Laboratory of Strongly-Coupled Quantum Matter Physics, and Department of Physics, University of Science and Technology of China, Hefei, Anhui 230026, China*
[2]*College of Physics, Hebei Normal University, Shijiazhuang, Hebei 050024, China*
[3]*Research Institute of Materials Science, and School of Chemistry and Materials Science, Shanxi Normal University, Linfen, Shanxi 041004, China*

The interlayer antiferromagnetic coupling hinders the observation of quantum anomalous Hall effect in magnetic topological insulator MnBi$_2$Te$_4$. We demonstrate that interlayer *ferromagnetism* can be established by utilizing the *p*-doping method in MnBi$_2$Te$_4$ multilayers. In two septuple layers system, the interlayer ferromagnetic coupling appears by doping nonmagnetic elements (e.g., N, P, As, Na, Mg, K, and Ca), due to the redistribution of orbital occupations of Mn. We further find that Mg and Ca elements are the most suitable candidates because of their low formation energy. Although, the *p*-doped two septuple layers exhibit topologically trivial band structure, the increase of layer thickness to three (four) septuple layers with Ca (Mg) dopants leads to the formation of the quantum anomalous Hall effect. Our proposed *p*-doping strategy without introducing additional magnetic disorder not only makes MnBi$_2$Te$_4$ become an ideal platform to realize the high-temperature quantum anomalous Hall effect without external magnetic field, but also can compensate the electrons from the intrinsic *n*-type defects in MnBi$_2$Te$_4$.

I. INTRODUCTION

Quantum anomalous Hall effect (QAHE) is a typical topological quantum phenomena with quantized Hall resistance and vanishing longitudinal resistance in the absence of external magnetic field [1–3]. It is promising in designing low-power electronic devices due to its dissipationless electronic transport properties. Although it was first theoretically proposed by Haldane in 1988 [4], the exploration of the QAHE began to attract huge interest ever since the first exfoliation of monolayer graphene in 2004 [5]. After that, there have been various proposed recipes in designing the QAHE [6–17], among which the magnetic topological insulator is the most favorable system by both theoretical and experimental studies due to its inherently strong spin-orbit coupling [18,19]. To realize the QAHE, the ferromagnetism is prerequisite and can be engineered by magnetic doping [9,20–26]. It was indeed theoretically proposed [9] in 2010 and later experimentally observed in 2013 in the magnetically doped topological insulator thin films [27–31]. However, the major obstacle, hindering the practical applications of QAHE, is the extremely low QAHE-observation temperature. Therefore, more efforts are being made to increase the QAHE observation temperature via various doping schemes in topological insulators [24–26].

Alternatively, MnBi$_2$Te$_4$, composed of septuple-layer (SL) blocks stacking along the [0001] direction via van der Waals

interaction [see Figs. 1(a) and 1(b)], becomes an appealing host material to realize exotic topological phases [32–35]. It exhibits intrinsic magnetism, following the A-type antiferromagnetic order, where the neighboring ferromagnetic Mn layers are coupled in an antiparallel manner [33,34]. It was reported that the QAHE can be observed at 6.5 K in a five-SL MnBi$_2$Te$_4$ flake, when an external magnetic field is applied; while the zero-field QAHE can only be observed at 1.4 K with ultrahigh sample quality [36,37]. The sensitivity of the QAHE on the sample quality indicates that the interlayer antiferromagnetic coupling is a critical obstacle in the QAHE formation, and the interlayer ferromagnetism is highly desired. The interlayer magnetic coupling of van der Waals materials is determined by the *d*-orbital occupation of transition metals [38–40]. One approach to manipulate the interlayer ferromagnetism is by stacking different *d*-orbital occupied van der Waals materials, e.g., MnBi$_2$Te$_4$/V(Eu)Bi$_2$Te$_4$ [39,40]. As demonstrated in below, another most efficient approach is by directly doping nonmagnetic *p*-type elements into MnBi$_2$Te$_4$.

In this work, we provide a systematic study on the magnetic and electronic properties of nonmagnetic *p*-doped MnBi$_2$Te$_4$ multilayers by using first-principles calculation methods. In two-SL MnBi$_2$Te$_4$, the interlayer ferromagnetic coupling can be realized by doping various nonmagnetic *p*-type elements (e.g., N, P, As, and Na, Mg, K, Ca) with the Curie temperature up to $T_C = 54$ K. The underlying physical origin is the redistribution of *d*-orbital occupation of Mn element induced hopping channels between t$_{2g}$ and e$_g$ from different SLs. Although it is topologically trivial in the

*Correspondence author: qisf@hebtu.edu.cn
†Correspondence author: xuxh@dns.sxnu.edu.cn
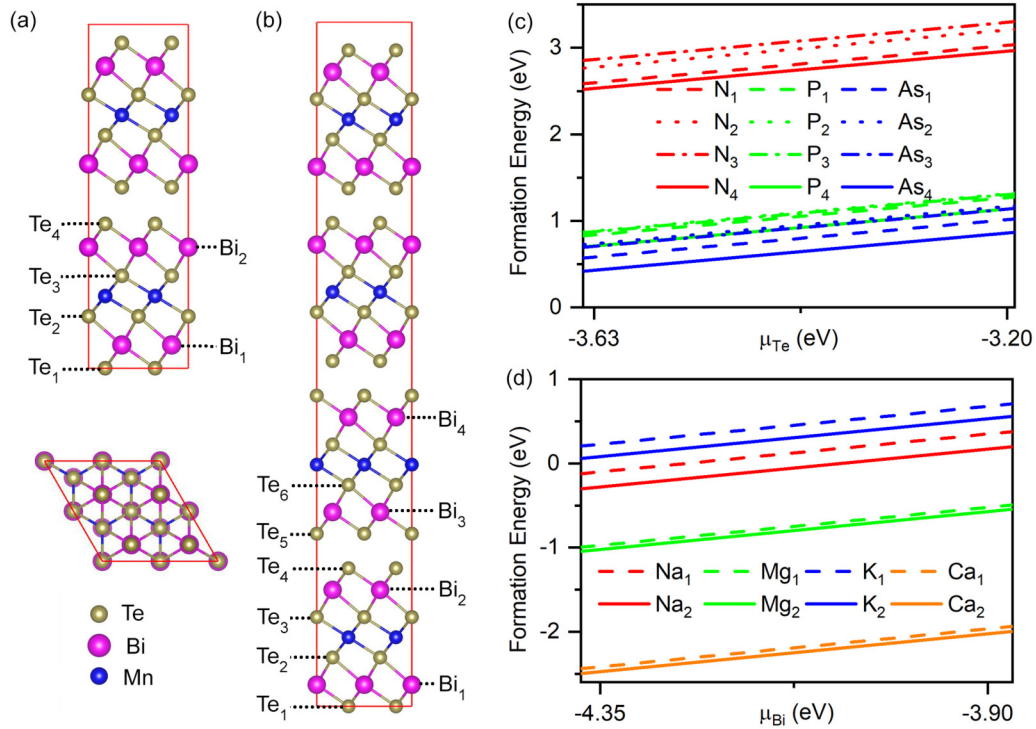‡Correspondence author: qiao@ustc.edu.cn

FIG. 1. Top view and side views of crystal structures of 2-4 SLs $MnBi_2Te_4$ and formation energies of p-type doped systems. (a) Two-SL $MnBi_2Te_4$ with one N/P/As substitution at sites Te_1-Te_4, or one Na/Mg/K/Ca substitution at sites Bi_1-Bi_2; (b) The 3-4 SLs $MnBi_2Te_4$ with one N/P/As substitution at sites Te_1-Te_6, or one Na/Mg/K/Ca substitution at sites Bi_1-Bi_4. [(c) and (d)] Formation energies of (c) N/P/As or (d) Na/Mg/K/Ca doped two-SL $MnBi_2Te_4$ as a function of the host element chemical potentials.

p-doped two-SL case, the topological phase transition occurs to harbour the high-temperature QAHE with a Chern number of $\mathcal{C} = -1$ when the system thickness is increased, i.e. Ca-doped three-SL, and Ca/Mg-doped four-SL $MnBi_2Te_4$, with the interlayer ferromagnetism still being preserved. Our work demonstrates a p-doping mechanism in producing ferromagnetism in $MnBi_2Te_4$ to form the high-temperature QAHE, which is experimentally accessible.

II. CALCULATION METHODS

Our first-principles calculations are performed by using the projected augmented-wave method [41] as implemented in the Vienna *ab initio* simulation package (VASP) [42,43]. The generalized gradient approximation (GGA) of the Perdew-Burke-Ernzerhof type is utilized to treat the exchange-correlation interaction [44]. In our calculations, the lattice constant of $MnBi_2Te_4$ is chosen as the experimental value of $a_0 = 4.33$ Å [45]. We use zero damping DFT-D3 method [46,47] to describe the van der Waals interaction of adjacent SLs of $MnBi_2Te_4$. All atoms are allowed to move during the structural optimization. The kinetic energy cutoff and energy convergence threshold are set to be 450 and 10^{-6} eV, respectively. The Hellmann-Feynman force tolerance criterion for convergence is 0.01 eV/Å. The Gaussian smearing method with a smearing width of 0.01 eV is adopted. A vacuum space of 20 Å is considered to avoid interaction between neighboring slabs. A Γ-centered $7 \times 7 \times 1$ ($5 \times 5 \times 1$) k mesh is adopted for the 2×2 (3×3) supercell. The $3d$ states of Mn are treated with GGA+U approach [48,49], with U =

5.34 eV, as in previous studies [50,51]. The topological related quantities are calculated by constructing maximally localized Wannier function as implemented in the Wannier90 package [52]. The Curie temperature T_C was estimated within the mean-field approximation $k_B T_C = 2/3Jx$ [53], where k_B is the Boltzmann constant, x is the dopant concentration, and J is the exchange parameter obtained from the total energy difference between ferromagnetic and antiferromagnetic configurations in different heterostructures. The phonon spectrum calculations are carried out by using the density functional perturbation theory as implemented in the PHONOPY package [54].

III. p-TYPE DOPING SCHEME IN $MnBi_2Te_4$

It was known that interlayer magnetic coupling in $MnBi_2Te_4$ is dominated by p-orbital mediated superexchange interaction, while d-orbital occupation has vital influence on the sign of interlayer magnetic coupling [39,40]. Based on the superexchange mechanism, doping p-type nonmagnetic elements can change the d-orbital occupation of Mn in the same SL. With the aid of hopping channel between $3d$-orbital of Mn in undoped SL and virtual $3d$-orbitals of Mn in p-doped SL, the interlayer ferromagnetic coupling becomes possible. In experiments, $MnBi_2Te_4$ was found to be electron-doping due to their intrinsic n-type defects [33]. Therefore another natural benefit of p-doping is the charge-compensation, which is a prerequisite for realizing the QAHE.

We now first study the possibility of p doping in $MnBi_2Te_4$ multilayers. Substituting Te/Bi atoms by
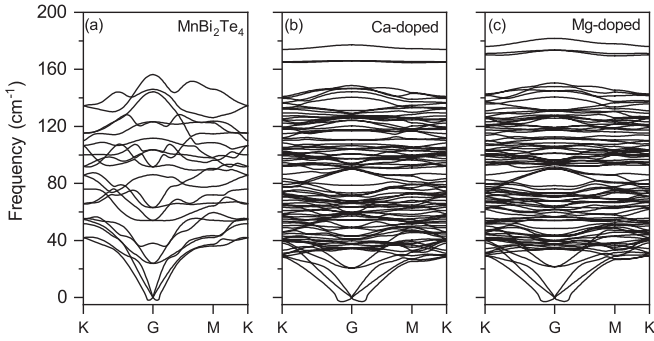
FIG. 2. Phonon dispersions of monolayer $MnBi_2Te_4$ with (a) pristine structure, (b) Ca dopant and (c) Mg dopant. A 2×2 $MnBi_2Te_4$ supercell is used to calculate phonon dispersion of Ca/Mg doped system.

nonmagnetic dopants is experimentally feasible, as implemented in Bi_2Te_3-family topological insulators. The Te and Bi elements in $MnBi_2Te_4$ exhibit respectively 2^- and 3^+ valence states. In order to employ p-doping, the corresponding substituted elements can be 3^-, 1^+, and 2^+ valence states, respectively. Therefore, the typical candidates of p-type nonmagnetic dopants include N/P/As for Te sites, or Na/Mg/K/Ca for Bi sites. As displayed in Fig. 1(a) for a two-SL $MnBi_2Te_4$, there are four Te substitutional sites (i.e., Te_1, Te_2, Te_3, Te_4), and two Bi substitutional sites (i.e., Bi_1, Bi_2). The formation energies can be evaluated from the expression [55–57]: $\Delta H_F = E_{tot}^D - E_{tot} - \sum n_i \mu_i$, where E_{tot}^D, E_{tot} are respectively the total energies of the p-doped and undoped systems, μ_i is the chemical potential for species i (host atoms or dopants), and n_i is the corresponding number of atoms added to or removed from the system.

Considering the formation energies of N/P/As substitutions at Te sites in one SL as displayed in Fig. 1(c), one can find that the Te_4 site is preferred. The formation energy of N substitution (2.5–3.0 eV) is larger than that of either P (0.6–1.2 eV) or As (about 0.4–1.0 eV). For Na/Mg/K/Ca substitutions at Bi sites in Fig. 1(d), one can find that the Bi_2 site is preferred, and the formation energies of Bi-site substitutions are always lower than those of Te-site substitutions. In particular, the formation energies of Na/Mg/Ca-substituted Bi_2 site are negative, suggesting that these dopings are experimentally feasible. As far as we know, the C-doped ZnO can also be experimentally realized, even thought the estimated formation energy of C substituted O in ZnO is about 5.3 eV [58], which is larger than those of aforementioned p-type dopants in $MnBi_2Te_4$. Moreover, phonon dispersions of two most feasible dopants, i.e., Mg and Ca, are calculated as displayed in Fig. 2, which suggests the stability of p-doped $MnBi_2Te_4$ systems. Hereinbelow, we concentrate on the most stable substitional sites (i.e., Te_4 and Bi_2) to study the magnetic and electronic properties of p-doped two-SL $MnBi_2Te_4$.

IV. INTERLAYER FERROMAGNETISM FROM p-DOPING

Figures 3(a) and 3(b) display the energy differences ($\Delta_E = E_{FM} - E_{AFM}$) between interlayer ferromagnetic (FM) and antiferromagnetic (AFM) states of the optimal configurations at different p-doped concentrations in two-SL $MnBi_2Te_4$.
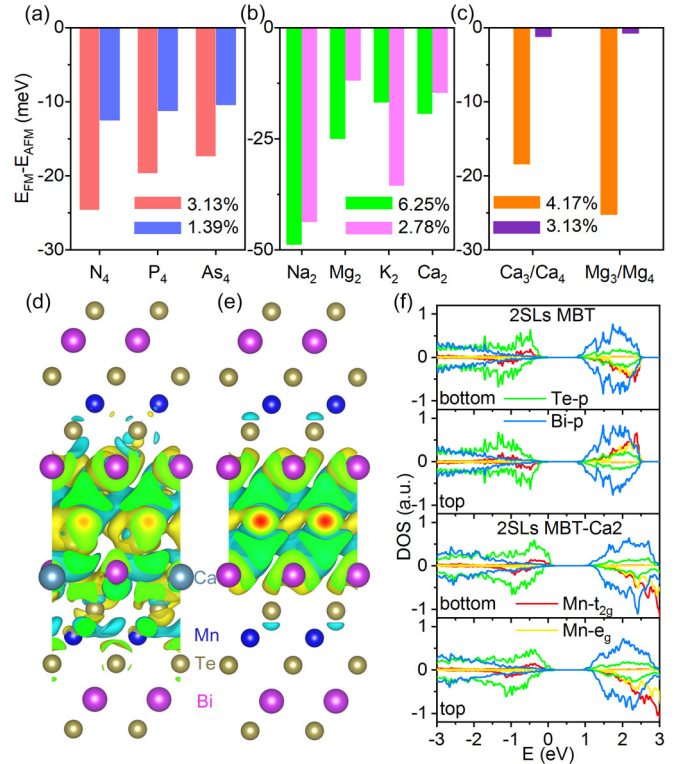

FIG. 3. [(a)–(c)] The energy differences between interlayer ferromagnetic (FM) and interlayer antiferromagnetic (AFM) states of the optimal configurations in (a) N/P/As doped two-SL $MnBi_2Te_4$ at 3.13% and 1.39% concentrations, (b) Na/Mg/K/Ca doped two-SL $MnBi_2Te_4$ at 6.25% and 2.78% concentrations, (c) Mg/Ca doped 3-4 SLs $MnBi_2Te_4$ at 4.17% and 3.13% concentrations. [(d) and (e)] Differential charge density of (d) Ca doped and (e) pristine two-SL $MnBi_2Te_4$. Yellow and green isosurface represent respectively charge accumulation and reduction. (f) Local density of states of Ca doped and pristine two-SL $MnBi_2Te_4$. Te-p, Bi-p, and Mn-d orbitals [t_{2g} and e_g] in each SL of $MnBi_2Te_4$ are displayed.

In the absence of doping, the two-SL $MnBi_2Te_4$ indeed exhibits interlayer antiferromagnetism (see Table I). The introduction of p-type dopants leads to $\Delta_E < 0$, strongly indicating that interlayer ferromagnetic state is more stable than the interlayer antiferromagnetic state. For N/P/As doping at Te_4 site [see Fig. 3(a)], Δ_E change respectively from $-12.4/-11.2/-10.3$ meV to $-24.5/-19.5/-17.2$ meV, along with the increase of doping concentration. For Na/Mg/K/Ca substitution at Bi_2 site [see Fig. 3(b)], Δ_E are respectively $-43.5/-11.8/-35.4/-14.5$ meV at 2.78% doping concentration, and $-48.6/-24.9/16.7/-19.2$ meV at 6.25% doping concentration.

Besides the energy difference for optimal doping sites, we also investigate magnetic properties of the remaining doping sites. Figure 4 displays the Δ_E of different configurations in p-doped two-SL $MnBi_2Te_4$. One can find that all p-doped systems prefer interlayer ferromagnetic coupling, and the doping sites near the van der Waals gap (e.g., Te_4 for N/P/As, Bi_2 for Na/Mg/K/Ca) exhibit much larger ferromagnetic coupling strength.

In addition, the ferromagnetic Curie temperature plays a crucial role in determining the QAHE observation
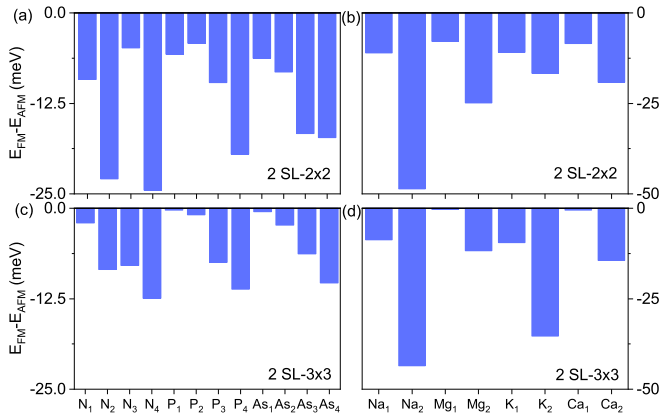
FIG. 4. The energy differences between interlayer ferromagnetic(FM) and interlayer antiferromagnetic (AFM) states of different configurations in N/P/As doped two-SL $MnBi_2Te_4$ at (a) 3.13% and (c) 1.39% doping concentrations. Na/Mg/K/Ca doped two-SL $MnBi_2Te_4$ at (b) 6.25% and (d) 2.78% doping concentrations.

temperature. The estimated Curie temperature from mean-field theory is listed in Table I, which ranges between 15.7 and 53.7 K depending on the dopants. For example, the Curie temperature of Ca-doped $MnBi_2Te_4$ can reach $T_C = 21.2$ K at 6.25% doping concentration, which can be further raised with the increase of doping concentration. Note that the higher doping concentration may decrease the spin-orbit coupling of the whole system.

For thicker $MnBi_2Te_4$ films (i.e., three-SL and four-SL films), we calculate the Δ_E of two most favorable dopants (Mg and Ca). For different substitutional sites, it is found that Bi_3 (Bi_4) site is most stable in three-SL (four-SL) $MnBi_2Te_4$ films. And for different magnetic configurations of the most stable doping site, the energy differences show that the ferromagnetic states are preferred (see Tables II and III). Figure 3(c) displays the energy difference Δ_E of one Mg or Ca dopant at Bi_3 (Bi_4) site in 2×2 supercells of three-SL (four-SL) $MnBi_2Te_4$. One can see that ferromagnetic coupling strength is dependent on doping concentration that is determined by the number of layers, i.e., for one dopant the increase of septuple layers leads to rapidly decrease of ferromagnetic coupling strength. Therefore larger ferromagnetic coupling strength in a multilayer system requires higher p-type doping concentration.

The formation mechanism of interlayer ferromagnetic coupling can be explained from the differential charge density and local density of states. Let us take the Ca-doped two-SL $MnBi_2Te_4$ as an example [see in Fig. 3(d)]. In the pristine case [see Fig. 3(e)], the charge distribution in the top SL is the same as that in the bottom SL. After Ca-doping in bottom SL, the charge of Mn atoms in the same SL is clearly decreased whereas that in top SL remains nearly unchanged. Such a charge redistribution leads to new hopping channels between Mn atoms in adjacent SLs. In pristine case, the t_{2g} and e_g orbitals are fully occupied, leading to the absence of electron hopping between t_{2g} and e_g orbitals. While as displayed in Fig. 3(f), the decrease of d-orbital occupation in bottom SL generates new hopping channels from t_{2g} (top SL) to e_g (bottom SL) and e_g (top SL) to e_g (bottom SL),
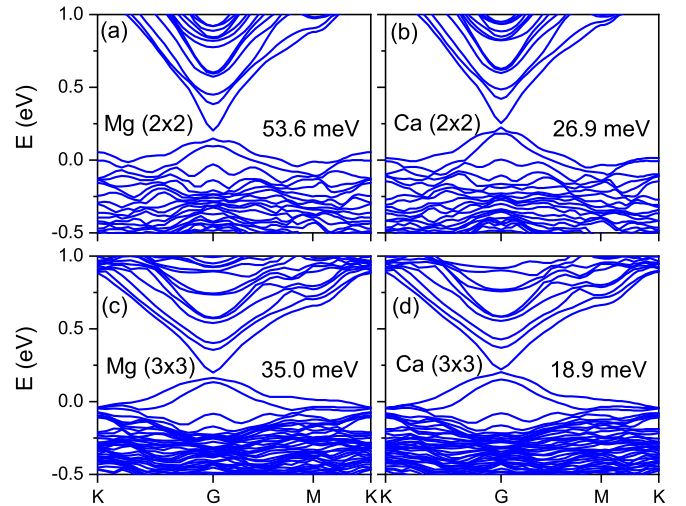

FIG. 5. Band structures and corresponding band gaps of Mg- and Ca-doped 2 SLs $MnBi_2Te_4$ with optimal configurations along high-symmetry lines. [(a) and (b)] Doping one Mg or Ca atom in 2×2 two-SL $MnBi_2Te_4$ with the concentration of 6.25%. [(c) and (d)] Doping one Mg or Ca atom in 3×3 two-SL $MnBi_2Te_4$ with the concentration of 2.78%.

which are allowed for ferromagnetic coupling. In addition, in Fig. 3(f), one can also find that a large spin polarization appears in the Te element after Ca doping, which suggests that the interlayer ferromagnetic coupling in Ca-doped two-SL $MnBi_2Te_4$ is mediated via the interlayer Te-Te superexchange interaction.

V. ELECTRONIC STRUCTURES AND TOPOLOGICAL PROPERTIES

Next, we explore the electronic band structures of the Mg and Ca doped multi-SL $MnBi_2Te_4$ (see Figs. 10 and 11 for band structures of other p dopants). Figure 5 displays the band structure along high-symmetry lines of the optimal configurations of Mg and Ca doped two-SL $MnBi_2Te_4$. As illustrated in Figs. 5(a) and 5(b), a band gap about 53.6 meV (26.9 meV) opens at Γ point with Mg (Ca) dopant for a doping concentration of 6.25%. When the doping concentration reduces to 2.78%, the band gap decreases to about 35.0 meV (18.9 meV) for Mg (Ca) dopant [see Figs. 5(c) and 5(d)]. To verify whether such a gap can host the QAHE or not, one can directly calculate the anomalous Hall conductance σ_{xy} by integrating Berry curvature of the occupied valence bands [59,60]. Unfortunately, we obtained $\sigma_{xy} = 0e^2/h$ for all p-doped two-SL $MnBi_2Te_4$, indicating that it is still a topological trivial phase, even though the ferromagnetism is well established. The possible reasons include: (i) the decrease of spin-orbit coupling originated from the light doping elements, and (ii) the film thickness influence [37,51]. To address these concerns, we first choose to dope some heavy metal elements (i.e., Sn, Pb, In, Tl) in two-SL $MnBi_2Te_4$ systems. As displayed in Table I, doping In or Tl results in the interlayer anti-ferromagnetic coupling; whereas although doping Sn or Pb gives rise to interlayer ferromagnetic coupling, no band gap opens at moderate doping concentrations (see Fig. 10).
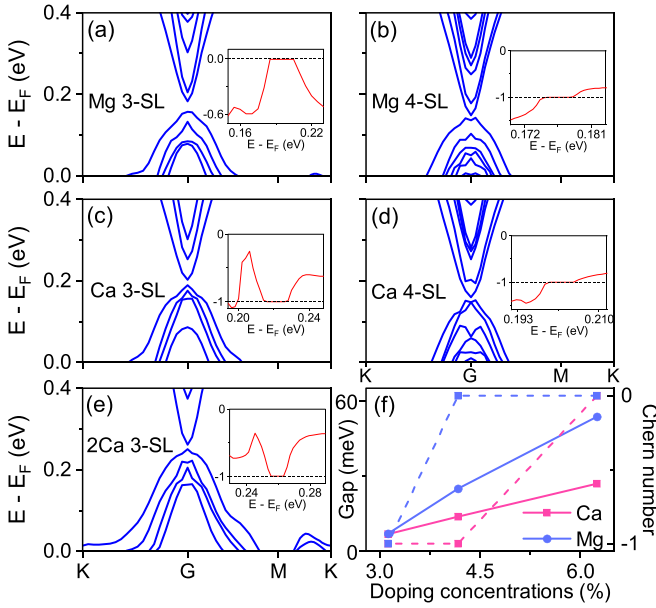
FIG. 6. Band structures along high-symmetry lines of MnBi$_2$Te$_4$ doped with Mg in (a) three-SL and (b) four-SL, doped with Ca in (c) three-SL and (d) four-SL, and (e) doped with two Ca in three-SL. The inset displays the anomalous Hall conductivity as a function of Fermi energy. (f) The dependence of band gap (solid lines) and Chern number (dashed lines) on the doping concentrations of Mg/Ca. The decrease of doping concentration indicates the increase of number of MnBi$_2$Te$_4$ SL.

We then consider the influence of film thickness of MnBi$_2$Te$_4$ in below.

Figures 6(a) and 6(b) display respectively the band structures of Mg-doped three- and four-SL MnBi$_2$Te$_4$, where the corresponding band gaps are respectively 24.9 meV (at 4.17% doping concentration) and 7.0 meV (at 3.13% doping concentration). The Hall conductance σ_{xy} evaluation gives respectively 0 and -1 in the units of e^2/h for three-SL and four-SL Mg-doped systems, strongly signaling a topological phase transition from trivial insulator to the QAHE with the increase of film thickness. For the Ca-doped cases as displayed in Figs. 6(c) and 6(d), one can see that the band gaps are respectively 13.7 meV (three-SL) and 6.8 meV (four-SL). Surprisingly, the Hall conductance in the band gap is $\sigma_{xy} = -e^2/h$ for both three- and four-SL Ca-doped MnBi$_2$Te$_4$. Therefore the increase of film thickness can lead to a topological phase transition in p-doped MnBi$_2$Te$_4$ multilayers. which can be attributed to magnetic Weyl semimetal nature of ferromagnetic MnBi$_2$Te$_4$, as observed in similar systems with thickness dependent Chern number [37,39].

For three-SL Ca-doped system, we also investigate the role of doping concentration on the electronic properties by including two Ca dopants at different substitutional sites. We find that all the calculated configurations display interlayer ferromagnetism, and Ca$_2$Ca$_4$ doped configuration is preferred with the Curie temperature of 52 K (see Fig. 12 and Table IV). As illustrated in Fig. 6(e), the band gap slightly decreases to 11.2 meV, with the nontrivial topology being preserved, but the Curie temperature is greatly enhanced from 20.3 K (one Ca dopant) to 52.0 K (two Ca dopants). Figure 6(f)
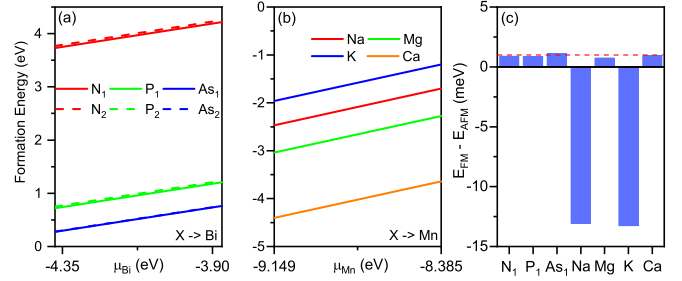

FIG. 7. [(a) and (b)] Formation energies of (a) N/P/As or (d) Na/Mg/K/Ca doped two-SL MnBi$_2$Te$_4$ as a function of the host element chemical. (c) The energy differences between interlayer ferromagnetic(FM) and interlayer antiferromagnetic (AFM) states of the most stable configurations in (a) and (b). The red dashed line represents energy difference of pristine two-SL MnBi$_2$Te$_4$ as a reference.

summarizes the band gaps and Hall conductance as functions of doping concentration. Compared with Mg dopant, the Ca doped MnBi$_2$Te$_4$ is preferred since that the topological phase appears in system with thinner thickness. Therefore the Mg- and Ca-doped MnBi$_2$Te$_4$ multilayers are beneficial for realizing the high-temperature QAHE.

VI. FORMATION ENERGIES AND MAGNETIC PROPERTIES OF ANTISITE SUBSTITUTIONS

In above, we have studied formation energies of N/P/As substitutions at Te sites and Na/Mg/K/Ca substitutions at Bi sites. Here we consider two type of representative antisite substitutions, i.e., N/P/As substitutions at Bi sites and Na/Mg/K/Ca substitutions at Mn sites. Figures 7(a) and 7(b) display the corresponding formation energies as a function of the host element chemical potentials. We can observe that the Bi$_1$ site is preferred for N/P/As substitutions and the positive formation energies is similar to that of N/P/As substitutions at Te sites as displayed in Fig. 1(c). For Na/Mg/K/Ca substitutions at Mn sites, the formation energies is also negative. It is
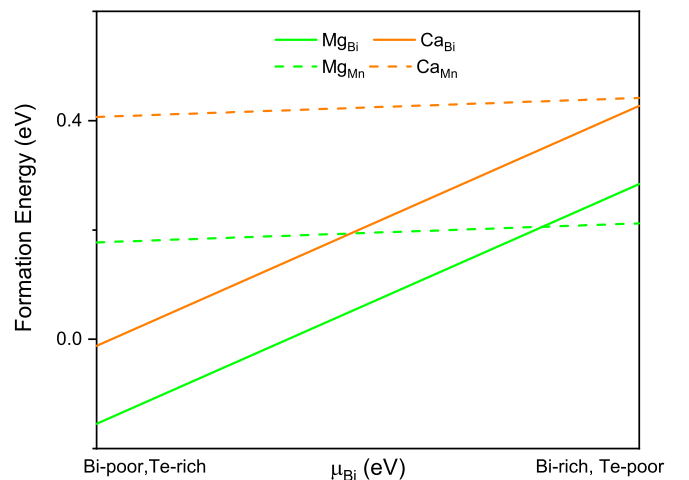

FIG. 8. Formation energies of Na/Mg/K/Ca doped Bi/Mn in two-SL MnBi$_2$Te$_4$. The chemical potentials of Na/K/Mg/Ca are evaluated by choosing Na$_2$Te, K$_2$Te, MgTe, and CaTe as reference.
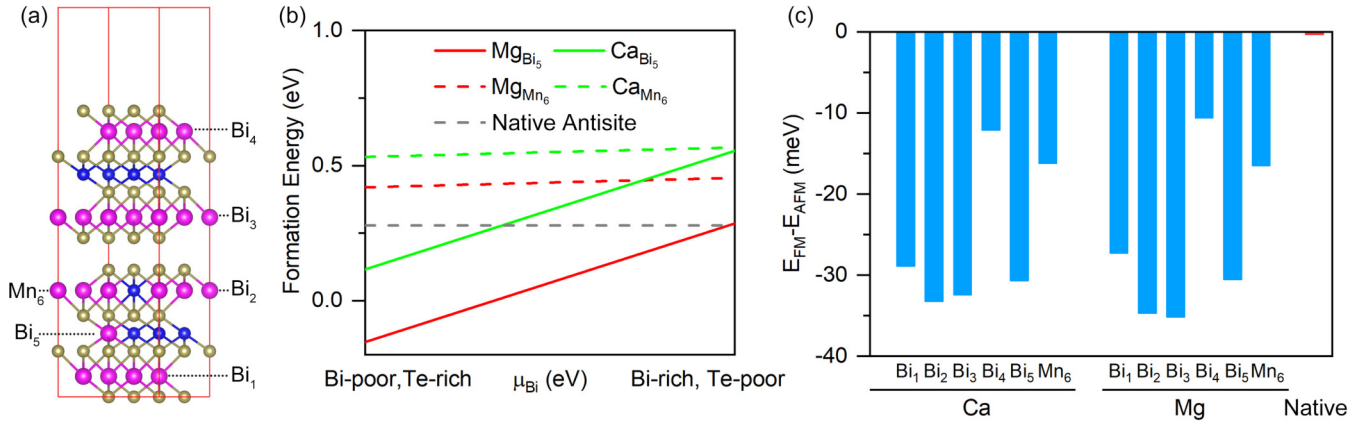
FIG. 9. (a) Two-SL MnBi$_2$Te$_4$ with one pair of native antisite defect Mn$_{Bi}$ and Bi$_{Mn}$. The six substitutional sites are labeled as Bi$_1$-Bi$_5$ and Mn$_6$. (b) Formation energies of Mg/Ca substitutions at the most stable Bi$_5$ site and at Mn site. The gray dashed line represents formation energy of native antisite defect. (c) The energy differences between interlayer ferromagnetic(FM) and interlayer antiferromagnetic (AFM) states of the six configurations doped with Mg/Ca. The presence of native antisite defect displays weak FM coupling with energy difference of ~ -0.32 meV.

worth noting that the chemical potentials from single element are usually larger than that from compound, resulting in a slightly underestimated formation energy. To quantitatively compare the formation energies of Mg/Ca dopants in Bi/Mn sites, we choose MgTe and CaTe as reference to evaluate the chemical potentials of Mg/Ca. Figure 8 displays formation energies of Mg/Ca doped Bi/Mn in two-SL MnBi$_2$Te$_4$. We can find that formation energy for dopants at Bi site is lower than that at Mn site in almost all range, indicating that Bi site is preferred for Mg/Ca dopants.

Figure 7(c) shows the corresponding energy difference between FM and AFM states. The presence of N/P/As substitutions at Bi sites does not obviously change the AFM coupling compared with pristine two-SL MnBi$_2$Te$_4$. For Na and K, the substitutions at Mn site displays interlayer FM coupling due to different valence states between Na/K (1^+) and Mn (2^+) elements induced charge redistribution. For Mg

and Ca substitutions at Mn site, interlayer AFM coupling is preserved since the same valence states between Mg/Ca and Mn elements. These results indicate that, even if Mg/Ca substitutions at Mn sites, the magnetic coupling strength of MnBi$_2$Te$_4$ is almost unchanged. Therefore the p-dopant at Bi sites plays a crucial role in determining magnetism of MnBi$_2$Te$_4$.

Besides above antisite substitutions, we also explore the doping possibility in the presence of native antisite defect, i.e., Mn$_{Bi}$ and Bi$_{Mn}$. Figure 9(a) displays the six substitutional sites labeled as Bi$_1$-Bi$_5$ and Mn$_6$. We find that Bi$_5$ site are preferred for Bi substitution. Formation energies of dopants at Bi$_5$ and Mn$_6$ sites are shown in Fig. 9(b), where formation energy of the native antisite defect Mn$_{Bi}$ and Bi$_{Mn}$ is depicted in gray for comparison [The MgTe and CaTe are chosen as reference to evaluate the chemical potentials of Mg/Ca]. We can observed that Mg/Ca substitutions at Bi sites have lower formation
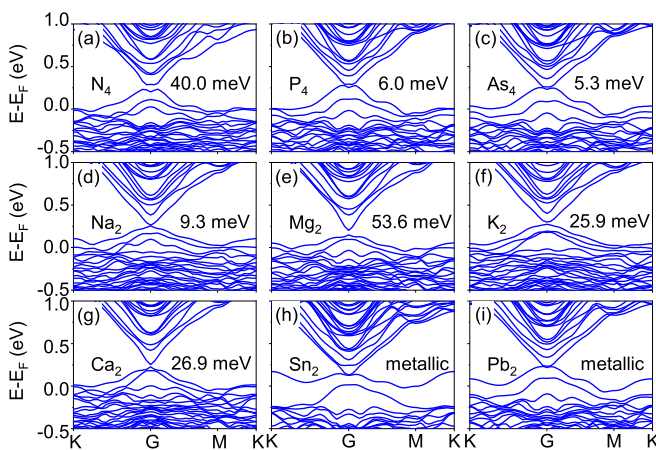

FIG. 10. Band structures and corresponding band gaps of p-doped two-SL (2×2) MnBi$_2$Te$_4$ with optimal configurations along high-symmetry lines. (a)–(i) are respectively for N, P, As, Na, Mg, K, Ca, Sn, and Pb doped two-SL MnBi$_2$Te$_4$. The doping concentrations are respectively 3.13% and 6.25% for substituted Te and Bi sites.

FIG. 11. Band structures and corresponding band gaps of p-doped two-SL (3×3) MnBi$_2$Te$_4$ with optimal configurations along high-symmetry lines. (a)-(i) are respectively for N, P, As, Na, Mg, K, Ca, Sn, and Pb doped two-SL MnBi$_2$Te$_4$. The doping concentrations are respectively 1.39% and 2.78% for substituted Te and Bi sites.
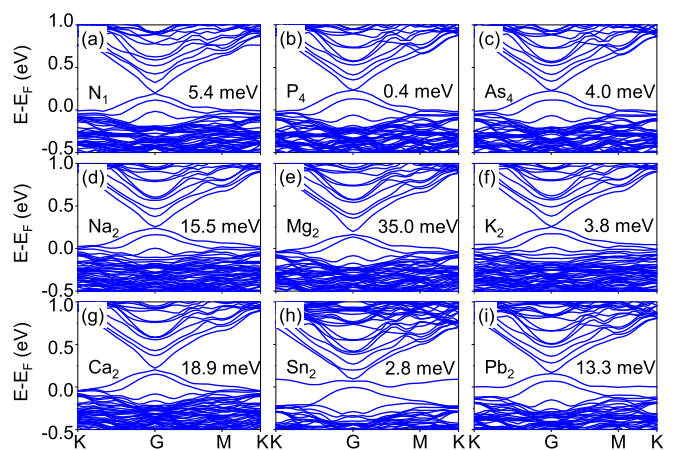
TABLE I. The band gap for the ground states, the energy difference $\Delta_E = E_{FM} - E_{AFM}$, and the estimated Curie temperature T_C of p-doped two-SL $MnBi_2Te_4$ with the optimal configurations. For 2×2 $MnBi_2Te_4$ supercell, the doping concentrations are respectively 3.13% and 6.25% for substituted Te and Bi sites. For 3×3 $MnBi_2Te_4$ supercell, the doping concentrations are respectively 1.39% and 2.78% for substituted Te and Bi sites. The red color indicates the antiferromagnetic ground state.

Structure	2×2 supercell			3×3 supercell		
	Gap (meV)	Δ_E (meV)	T_C (K)	Gap (meV)	Δ_E (meV)	T_C (K)
$N_4(N_1)$	40.0	−24.5	27.1	5.4	−2.0	2.3
P_4	6.0	−19.5	21.6	0.4	−11.2	12.3
As_4	5.3	−17.2	19.0	4.0	−10.3	11.4
Na_2	9.3	−48.6	53.7	15.5	−43.5	48.1
Mg_2	53.6	−24.9	27.5	35.0	−11.8	13.0
K_2	25.9	−16.7	18.4	3.8	−35.4	39.1
Ca_2	26.9	−19.2	21.2	18.9	−14.5	16.0
Sn_2	Metallic	−14.2	15.7	2.8	−14.3	15.8
Pb_2	Metallic	−17.1	18.9	13.3	−7.5	8.3
In_2	197.9	1.7	–	145.5	3.1	–
Tl_2	163.3	6.1	–	149.5	7.5	–
$MnBi_2Te_4$	80.0	1.0	–		2.3	–

energy than that at Mn sites, indicating that Bi site is preferred for Mg/Ca dopants in the presence of native antisite defect. Figure 9(c) displays the energy differences between interlayer FM and AFM states of the six configurations doped with Mg/Ca. In the presence of native antisite defect, the system demonstrates weak FM coupling (−0.32 meV), whereas the further inclusion of Mg/Ca dopants at Bi or Mn sites greatly enhances FM coupling strength of $MnBi_2Te_4$.

Based on the results displayed in this Section, we can conclude that (i) Mg/Ca substitutions at Bi sites are preferred than that at Mn sites; (ii) magnetic coupling strength of $MnBi_2Te_4$ is almost unchanged even if Mg/Ca substitutions at Mn sites; (iii) in the presence of native antisite defect, Mg/Ca doped system displays interlayer ferromagnetism regardless of the doping sites.

VII. SUMMARY

In conclusion, we propose that a feasible p-type doping strategy in $MnBi_2Te_4$ can be used to realize interlayer ferromagnetism and the high-temperature QAHE. We provide proof-of-principle numerical demonstration that (1) interlayer ferromagnetic transition can appear when some nonmagnetic p-type elements are doped into $MnBi_2Te_4$; (2) band structures and topological property calculations show that Ca- and Mg-

doped $MnBi_2Te_4$ multilayer can realize the QAHE with Chern number of $\mathcal{C} = -1$.

Experimentally, Mg, Ca and some nonmagnetic elements doped topological insulators have been successfully fabricated in order to tune carrier type and density [61–63]. For example, to compensate the n-type carrier induced by Se vacancies in topological insulator Bi_2Se_3, a small concentration of Ca is doped, and insulating behavior is preserved whereas the Fermi level is tuned into the band gap [61]. For the $MnBi_2Te_4$, from our calculation, the formation energies of Ca substitution are only −2.5 to −3.0 eV. Hence the p-type Ca dopants in $MnBi_2Te_4$ are very feasible in experiment. The merits of p-type doping in $MnBi_2Te_4$ is that it can not only result in interlayer ferromagnetic coupling without introducing additional magnetic disorder, but also compensate the intrinsic n-type carrier, which in principle guarantees the insulating state and is beneficial to realize the high-temperature QAHE in $MnBi_2Te_4$. Our work provide a highly desirable scheme to overcome the difficulty of the observing of the QAHE in $MnBi_2Te_4$ without applying external magnetic field.

TABLE II. The structural and magnetic properties of Ca/Mg doped three-SL $MnBi_2Te_4$ with doping concentration of 4.17%. The spin direction of each septuple layer is denoted by the up/down arrow. The ground state of each dopant is denoted by red. The energy differences between the specific structure and ground state are shown. The energy is in unit of meV.

Structure	$\Delta_E(\uparrow\downarrow\uparrow)$	$\Delta_E(\uparrow\uparrow\downarrow)$	$\Delta_E(\uparrow\downarrow\downarrow)$	$\Delta_E(\uparrow\uparrow\uparrow)$
Mg_1	91.0	84.1	91.8	84.7
Mg_2	46.9	24.5	44.9	24.7
Mg_3	25.1	6.3	20.9	0
Ca_1	107.3	99.0	108.1	100.3
Ca_2	50.6	35.3	48.3	34.2
Ca_3	18.3	3.2	15.0	0
$MnBi_2Te_4$	0	1.2	1.1	2.5

TABLE III. The structural and magnetic properties of Ca/Mg doped four-SL MnBi$_2$Te$_4$ with doping concentration of 4.17%. The spin direction of each septuple layer is denoted by the up/down arrow. The ground state of each dopant is denoted by red. The energy differences between the specific structure and ground state are shown. The energy is in unit of meV.

Structure	$\Delta_E(\uparrow\downarrow\uparrow\downarrow)$	$\Delta_E(\uparrow\uparrow\uparrow\downarrow)$	$\Delta_E(\uparrow\uparrow\downarrow\uparrow)$	$\Delta_E(\uparrow\uparrow\downarrow\downarrow)$	$\Delta_E(\uparrow\downarrow\uparrow\uparrow)$	$\Delta_E(\uparrow\downarrow\downarrow\uparrow)$	$\Delta_E(\uparrow\downarrow\downarrow\downarrow)$	$\Delta_E(\uparrow\uparrow\uparrow\uparrow)$
Mg$_2$	41.3	20.9	23.0	24.2	42.7	43.4	39.2	22.0
Mg$_3$	26.3	1.8	9.3	9.6	26.7	20.5	20.2	3.4
Mg$_4$	20.7	3.5	14.7	11.7	17.9	8.4	6.8	0
Ca$_2$	48.1	33.0	35.2	36.2	48.8	44.9	45.9	34.0
Ca$_3$	44.6	6.7	13.1	13.1	25.6	17.6	18.4	7.4
Ca$_4$	19.6	2.7	11.5	7.7	14.6	7.4	5.2	0
MnBi$_2$Te$_4$	0	1.9	0.9	1.8	0.9	0.9	1.8	2.8

APPENDIX A: BAND STRUCTURES OF *p*-DOPED TWO-SL MnBi$_2$Te$_4$

In Figs. 10 and 11, we plot the band structures of *p*-doped two-SL MnBi$_2$Te$_4$ with optimal configurations with different doping concentrations. In Fig. 10, we can observe that finite gaps are opened around Γ point except for Sn- and Pb-doped systems. When reduces doping concentration, as displayed in Fig. 11, one can find that the gaps for N/P/As/Na/Mg/K/Ca doped systems are decreased whereas small gaps exists for Sn/Pb doped systems.

In Table I, we summarize the band gap for the ground states, the energy difference $\Delta_E = E_{FM} - E_{AFM}$, and the estimated Curie temperature T$_C$ of *p*-doped two-SL MnBi$_2$Te$_4$ with the optimal configurations. Besides the *p*-doped systems showing interlayer ferromagnetism as discussed above, it is noteworthy that In/Tl heavy metal-doped MnBi$_2$Te$_4$ exhibits

a enhanced interlayer antiferromagnetic coupling compared with the pristine two-SL MnBi$_2$Te$_4$.

APPENDIX B: MAGNETIC PROPERTIES OF *p*-DOPED THREE- AND FOUR-SL MnBi$_2$Te$_4$

Table II displays the structural and magnetic properties of Ca/Mg doped three-SL MnBi$_2$Te$_4$ with doping concentration of 4.17%. The corresponding doping sites are shown in the main text. One can find that Bi$_3$ substitutional site is most stable, and the ferromagnetic ground state is preferred in Mg/Ca doped three-SL MnBi$_2$Te$_4$. For Ca/Mg doped four-SL MnBi$_2$Te$_4$, as shown in Table III, we can observe that Bi$_4$ substitutional site is most stable, and the ferromagnetic ground state is preserved.

APPENDIX C: STRUCTURAL AND MAGNETIC PROPERTIES OF THREE-SL MnBi$_2$Te$_4$ WITH TWO Ca DOPANTS

Figure 12(a) displays the possible substitutional sites for two Ca dopants in three-SL MnBi$_2$Te$_4$, where the sites near van der Waals gap are considered because they are more stable. Due to the inversion symmetry, there are four combinations of doping sites as shown in Table IV. We can find that the Ca$_2$Ca$_4$ doped configuration is most stable with interlayer ferromagnetic coupling, and the Curie temperature can approach 52 K.

APPENDIX D: MAGNETIC COUPLING WITH/WITHOUT SPIN-ORBIT COUPLING IN *p*-DOPED TWO-SL MnBi$_2$Te$_4$

In above magnetic coupling calculation, the spin-orbit coupling is not included. Fig. 12(b) displays the energy differences ΔE between FM and AFM states with/without
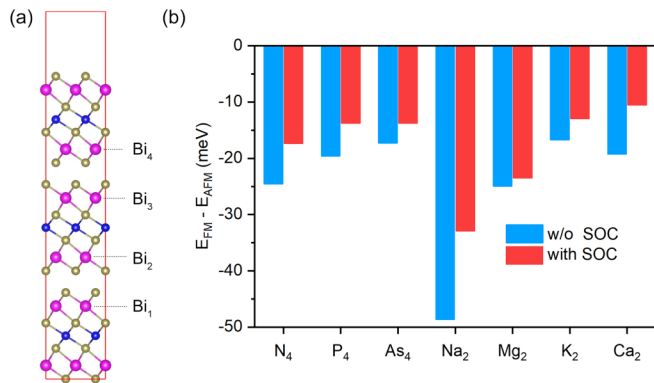

FIG. 12. (a) The substitutional sites for two Ca dopants in three-SL MnBi$_2$Te$_4$. (b) The comparison of energy differences between FM and AFM states with/without spin-orbit coupling in *p*-doped two-SL MnBi$_2$Te$_4$.

TABLE IV. The structural and magnetic properties of two Ca dopants in three-SL MnBi$_2$Te$_4$. The energy differences between the specific structure and ground state are shown. The ground state is denoted by red. The energy is in unit of meV.

Structure	$\Delta_E(\uparrow\downarrow\uparrow)$	$\Delta_E(\uparrow\uparrow\uparrow)$	T$_C$ (K)
Ca$_2$Ca$_4$	47.1	0	52.0
Ca$_1$Ca$_2$	130.0	98.2	35.1
Ca$_1$Ca$_4$	61.5	17.2	48.9
Ca$_2$Ca$_3$	98.0	42.6	61.3

spin-orbit coupling in p-doped two-SL $MnBi_2Te_4$. We can observe that, although the inclusion of spin-orbit coupling slightly increases the energy differences, the variation trend of ΔE is similar before/after spin-orbit coupling is considered for different dopants and the interlayer ferromagnetic coupling is preserved.

[1] H. Weng, R. Yu, X. Hu, X. Dai, and Z. Fang, Adv. Phys. **64**, 227 (2015).

[2] Y. Ren, Z. Qiao, and Q. Niu, Rep. Prog. Phys. **79**, 066501 (2016).

[3] K. He, Y. Wang, and Q.-K. Xue, Annu. Rev. Condens. Matter Phys. **9**, 329 (2018).

[4] F. D. M. Haldane, Phys. Rev. Lett. **61**, 2015 (1988).

[5] K. S. Novoselov, A. K. Geim, S. V. Morozov, D. Jiang, Y. Zhang, S. V. Dubonos, I. V. Grigorieva, and A. A. Firsov, Science **306**, 666 (2004).

[6] M. Onoda and N. Nagaosa, Phys. Rev. Lett. **90**, 206601 (2003).

[7] C. X. Liu, X. L. Qi, X. Dai, Z. Fang, and S. C. Zhang, Phys. Rev. Lett. **101**, 146802 (2008).

[8] C. Wu, Phys. Rev. Lett. **101**, 186807 (2008).

[9] R. Yu, W. Zhang, H. J. Zhang, S. C. Zhang, X. Dai, and Z. Fang, Science **329**, 61 (2010).

[10] Z. H. Qiao, S. A. Yang, W. X. Feng, W.-K. Tse, J. Ding, Y. G. Yao, J. Wang, and Q. Niu, Phys. Rev. B **82**, 161414(R) (2010).

[11] Z. F. Wang, Z. Liu, and F. Liu, Phys. Rev. Lett. **110**, 196801 (2013).

[12] K. F. Garrity and D. Vanderbilt, Phys. Rev. Lett. **110**, 116802 (2013).

[13] J. Hu, Z. Zhu, and R. Wu, Nano Lett. **15**, 2074 (2015).

[14] C. Fang, M. J. Gilbert, and B. A. Bernevig, Phys. Rev. Lett. **112**, 046801 (2014).

[15] J. Wang, B. Lian, H. Zhang, Y. Xu, and S. C. Zhang, Phys. Rev. Lett. **111**, 136801 (2013).

[16] G. F. Zhang, Y. Li, and C. Wu, Phys. Rev. B **90**, 075114 (2014).

[17] H. Z. Lu, A. Zhao, and S. Q. Shen, Phys. Rev. Lett. **111**, 146802 (2013).

[18] M. Z. Hasan and C. L. Kane, Rev. Mod. Phys. **82**, 3045 (2010).

[19] X. L. Qi and S. C. Zhang, Rev. Mod. Phys. **83**, 1057 (2011).

[20] T. Jungwirth, J. Sinova, J. Masek, J. Kurmancupcarera, and A. H. MacDonald, Rev. Mod. Phys. **78**, 809 (2006).

[21] Y. S. Hor, P. Roushan, H. Beidenkopf, J. Seo, D. Qu, J. G. Checkelsky, L. A. Wray, D. Hsieh, Y. Xia, S. Y. Xu, D. Qian, M. Z. Hasan, N. P. Ong, A. Yazdani, and R. J. Cava, Phys. Rev. B **81**, 195203 (2010).

[22] C. Niu, Y. Dai, M. Guo, W. Wei, Y. Ma, and B. Huang, Appl. Phys. Lett. **98**, 252502 (2011).

[23] P. P. J. Haazen, J. B. Laloe, T. J. Nummy, H. J. M. Swagten, P. Jarillo-Herrero, D. Heiman, and J. S. Moodera, Appl. Phys. Lett. **100**, 082404 (2012).

[24] S. Qi, Z. Qiao, X. Deng, E. D. Cubuk, H. Chen, W. Zhu, E. Kaxiras, S. B. Zhang, X. Xu, and Z. Zhang, Phys. Rev. Lett. **117**, 056804 (2016).

[25] X. Feng, Y. Feng, J. Wang, Y. Ou, Z. Hao, C. Liu, Z. Zhang, L. Zhang, C. Lin, J. Liao, Y. Li, L.-L. Wang, S.-H. Ji, X. Chen, X. Ma, S.-C. Zhang, Y. Wang, K. He, and Q.-K. Xue, Adv. Mater. **28**, 6386 (2016).

[26] Y. Ou, C. Liu, G. Y. Jiang, Y. Feng, D. Y. Zhao, W. X. Wu, X. X. Wang, W. Li, C. L. Song, L. L. Wang, W. B. Wang, W. D. Wu,

[27] C.-Z. Chang, J. S. Zhang, X. Feng, J. Shen, Z. C. Zhang, M. Guo, K. Li, Y. Ou, P. Wei, L.-L. Wang, Z.-Q. Ji, Y. Feng, S. H. Ji, X. Chen, J. F. Jia, X. Dai, Z. Fang, S.-C. Zhang, K. He, Y. Y. Wang *et al.* Science **340**, 167 (2013).

[28] J. G. Checkelsky, R. Yoshimi, A. Tsukazaki, K. S. Takahashi, Y. Kozuka, J. Falson, M. Kawasaki, and Y. Tokura, Nat. Phys. **10**, 731 (2014).

[29] X. Kou, S.-T. Guo, Y. Fan, L. Pan, M. Lang, Y. Jiang, Q. Shao, T. Nie, K. Murata, J. Tang, Y. Wang, L. He, T.-K. Lee, W.-L. Lee, and K. L. Wang, Phys. Rev. Lett. **113**, 137201 (2014).

[30] C. Z. Chang, W. Zhao, D. Y. Kim, H. Zhang, B. A. Assaf, D. Heiman, S.-C. Zhang, C. Liu, M. H. W. Chan, and J. S. Moodera, Nat. Mater. **14**, 473 (2015).

[31] M. Mogi, R. Yoshimi, A. Tsukazaki, K. Yasuda, Y. Kozuka, K. S. Takahashi, and Y. Tokura, Appl. Phys. Lett. **107**, 182401 (2015).

[32] D. Zhang, M. Shi, T. Zhu, D. Xing, H. Zhang, and J. Wang, Phys. Rev. Lett. **122**, 206401 (2019).

[33] Y. Gong, J. Guo, J. Li, K. Zhu, M. Liao, X. Liu, Q. Zhang, L. Gu, L. Tang, X. Feng, D. Zhang, W. Li, C. Song, L. Wang, P. Yu, X. Chen, Y. Wang, H. Yao, W. Duan, Y. Xu *et al.* Chin. Phys. Lett. **36**, 076801 (2019).

[34] J. Li, Y. Li, S. Du, Z. Wang, B. L. Gu, S.-C. Zhang, K. He, W. Duan, and Y. Xu, Sci. Adv. **5**, eaaw5685 (2019).

[35] H. Wang, D. Wang, Z. Yang, M. Shi, J. Ruan, D. Xing, J. Wang, and H. Zhang, Phys. Rev. B **101**, 081109(R) (2020).

[36] Y. Deng, Y. Yu, M. Z. Shi, J. Wang, X. H. Chen, and Y. Zhang, Science **367**, 895 (2020).

[37] J. Ge, Y. Liu, J. Li, H. Li, T. Luo, Y. Wu, Y. Xu, and J. Wang, Natl. Sci. Rev. **7**, 1280 (2020).

[38] J. W. Xiao and B. H. Yan, 2D Mater. **7**, 045010 (2020).

[39] Z. Li, J. Li, K. He, X. Wan, W. Duan, and Y. Xu, Phys. Rev. B **102**, 081107(R) (2020).

[40] W. Zhu, C. Song, L. Liao, Z. Zhou, H. Bai, Y. Zhou, and F. Pan, Phys. Rev. B **102**, 085111 (2020).

[41] P. E. Blöchl, Phys. Rev. B **50**, 17953 (1994).

[42] G. Kresse and J. Furthmuller, Phys. Rev. B **54**, 11169 (1996).

[43] G. Kresse and D. Joubert, Phys. Rev. B **59**, 1758 (1999).

[44] J. P. Perdew, K. Burke, and M. Ernzerhof, Phys. Rev. Lett. **77**, 3865 (1996).

[45] D. S. Lee, T.-H. Kim, C.-H. Park, C.-Y. Chung, Y. S. Lim, W.-S. Seoa, and H.-H. Park, CrystEngComm **15**, 5532 (2013).

[46] S. Grimme, J. Antony, S. Ehrlich, and H. Krieg, J. Chem. Phys. **132**, 154104 (2010).

[47] S. Grimme, S. Ehrlich, and L. Goerigk, J. Comput. Chem. **32**, 1456 (2011).

[48] V. I. Anisimov, J. Zaanen, and O. K. Anderson, Phys. Rev. B **44**, 943 (1991).

[49] S. L. Dudarev, G. A. Botton, S. Y. Savrasov, C. J. Humphreys, and A. P. Sutton, Phys. Rev. B **57**, 1505 (1998).

[50] M. M. Otrokov, T. V. Menshchikova, M. G. Vergniory, I. P. Rusinov, A. Y. Vyazovskaya, Y. M. Koroteev, G. Bihlmayer, A. Ernst, P. M. Echenique, and A. Arnau, 2D Mater. **4**, 025082 (2017)

[51] M. M. Otrokov, I. P. Rusinov, M. Blanco-Rey, M. Hoffmann, A. Y. Vyazovskaya, S. V. Eremeev, A. Ernst, P. M. Echenique, A. Arnau, and E. V. Chulkov, Phys. Rev. Lett. **122**, 107202 (2019).

[52] A. A. Mostofi, J. R. Yates, Y.-S. Lee, I. Souza, D. Vanderbilt, and N. Marzari, Comput. Phys. Commun. **178**, 685 (2008).

[53] L. Bergqvist, O. Eriksson, J. Kudrnovsky, V. Drchal, A. Bergman, L. Nordstrom, and I. Turek, Phys. Rev. B **72**, 195210 (2005).

[54] A. Togo and I. Tanaka, Scr. Mater. **108**, 1 (2015).

[55] J. M. Zhang, W. G. Zhu, Y. Zhang, D. Xiao, and Y. G. Yao, Phys. Rev. Lett. **109**, 266405 (2012).

[56] S. Qi, R. Gao, M. Chang, T. Hou, Y. Han, and Z. Qiao, Phys. Rev. B **102**, 085419 (2020).

[57] We choose the nitrogen molecule, white P4, rhombohedral As, body-centered-cubic (bcc) Na, bcc K, hexagonal Mg and Ca to evaluate the chemical potentials of these doping elements.

[58] H. Pan, J. B. Yi, L. Shen, R. Q. Wu, J. H. Yang, J. Y. Lin, Y. P. Feng, J. Ding, L. H. Van, and J. H. Yin, Phys. Rev. Lett. **99**, 127201 (2007).

[59] Y. G. Yao, L. Kleinman, A. H. MacDonald, J. Sinova, T. Jungwirth, D.-S. Wang, E. Wang, and Q. Niu, Phys. Rev. Lett. **92**, 037204 (2004).

[60] D. Xiao, M. C. Chang, and Q. Niu, Rev. Mod. Phys. **82**, 1959 (2010).

[61] Z. Wang, T. Lin, P. Wei, X. Liu, R. Dumas, K. Liu, and J. Shi, Appl. Phys. Lett. **97**, 042112 (2010).

[62] S. Byun, J. Cha, C. Zhou, Y. K. Lee, H. Lee, S. H. Park, W. B. Lee, and I. Chung, J. Solid State Chem. **269**, 396 (2019).

[63] J. Moon, Z. Huang, W. Wu, and S. Oh, Phys. Rev. Mater. **4**, 024203 (2020).